nature portfolio

https://doi.org/10.1038/s41586-026-10684-4

Supplementary information

Chiral laser gyroscopes breaking the lock-in limit

Supplementary Materials for

Chiral laser gyroscopes breaking the lock-in limit

Yuan-Hao Mao[1,2†*], Ji-Peng Xu[2,3†*], Hong-Teng Ji[2†], Li-Tian Yang[2], Zhong-Qi Tan[2], Yu-Chuan Quan[4], Tao Pu[1], Wei Shao[1], Jun-Quan Hu[1], Ran Huang[5], Franco Nori[5*], Hui Jing[6,7*]

This PDF file includes:

S1: Calculation of coefficients in He-Ne ring lasers **2**

S2: Analysis of the critical condition of chiral spontaneous symmetry breaking in a ring laser **5**

S3: Control strategies of the chiral ring laser gyroscope based on its output signal **9**

S4: Analysis of bias stability in the chiral RLG **12**

S5: Operating characteristics of the He-Ne ring laser **14**

References: **15**

S1: Calculation of coefficients in He-Ne ring lasers

Table S1 Descriptions of Parameters in Equation (1) in the main text

Classifications	Parameters	Physical Contents
Amplitude Parameters	r	Backscattering coupling coefficient
	α	Net gain coefficient
	β	Self-saturation coefficient
	θ	Cross-saturation coefficient
	$\boldsymbol{\xi = \theta/\beta}$	**Nonlinear coupling strength**
Frequency Parameters	Ω_{S}	Sagnac frequency shift
	σ	Frequency pulling coefficient
	ρ	Self-pushing coefficients
	τ	Cross-pushing coefficients
	$\boldsymbol{\eta = \rho - \tau}$	**Nonlinear frequency pulling**

The nonlinear coefficients ($\theta, \beta, \rho, \tau$) highlighted in gray in Table S1 determine the conditions for chiral SSB and the frequency bias characteristics in the ring laser gyroscope. Below, we calculate these coefficients based on the plasma dispersion function of the Ne gain medium. In the main text, θ/β and $(\rho-\tau)$ are defined as the nonlinear coupling strength ξ and the nonlinear frequency pulling coefficient η, respectively. Namely, $\xi = \theta/\beta$, and $\eta = \rho - \tau$.

To simplify the calculations, we first need to define the frequency parameter $\varepsilon = (\nu - \nu_0)/ku_0$, where ν_0 is the center frequency of the Ne^{20} gain profile, k is the wave number, u_0 is the most probable speed of the Ne^{20} atoms, and their product ku_0 is the width of the Doppler broadening. Then, the ratio of the homogeneous broadening γ to Doppler broadening is defined as κ (i.e., $\kappa = \gamma/ku$). The plasma dispersion function $Z(\varepsilon)$ can be derived as the following equation[1–3]:

$$Z(\varepsilon) = Z_{\mathrm{r}}(\varepsilon) + iZ_{\mathrm{i}}(\varepsilon) = 2i\int_{-\infty}^{+\infty} \exp(-x^2 - 2\kappa x + 2i\varepsilon x)\, dx \tag{S1}$$

where $Z_{\mathrm{r}}(\varepsilon)$ and $Z_{\mathrm{i}}(\varepsilon)$ are defined as the real and imaginary parts of $Z(\varepsilon)$, respectively. The nonlinear coefficients can be calculated through $Z(\varepsilon)$ in He-Ne ring lasers[1–3]:

$$\beta = g\left[Z_{\mathrm{i}}(\varepsilon) - \kappa\frac{dZ_{\mathrm{r}}(\varepsilon)}{d\varepsilon}\right] \tag{S2}$$

$$\theta = g\frac{\kappa^2}{\kappa^2+\varepsilon^2}Z_{\mathrm{i}}(\varepsilon) \tag{S3}$$

$$\rho = -g\frac{c}{2L}\kappa\frac{dZ_{\mathrm{i}}(\varepsilon)}{d\varepsilon} \tag{S4}$$

$$\tau = g\frac{c}{2L}\frac{\kappa\varepsilon}{\kappa^2+\varepsilon^2}Z_{\mathrm{i}}(\varepsilon) \tag{S5}$$

where g is the unsaturated gain coefficient, c is the speed of light, L is the length of the laser cavity. The calculations of the nonlinear parameters β, θ, ρ and τ are simplified here. For a complete and detailed derivation, readers can refer to Chapters 9 to 11 of *Laser Physics* (1978) written by Sargent, Scully and Lamb, or can find a similar theoretical framework in J. R. Wilkinson, Ring Lasers, Progress in Quantum Electronics (1987).

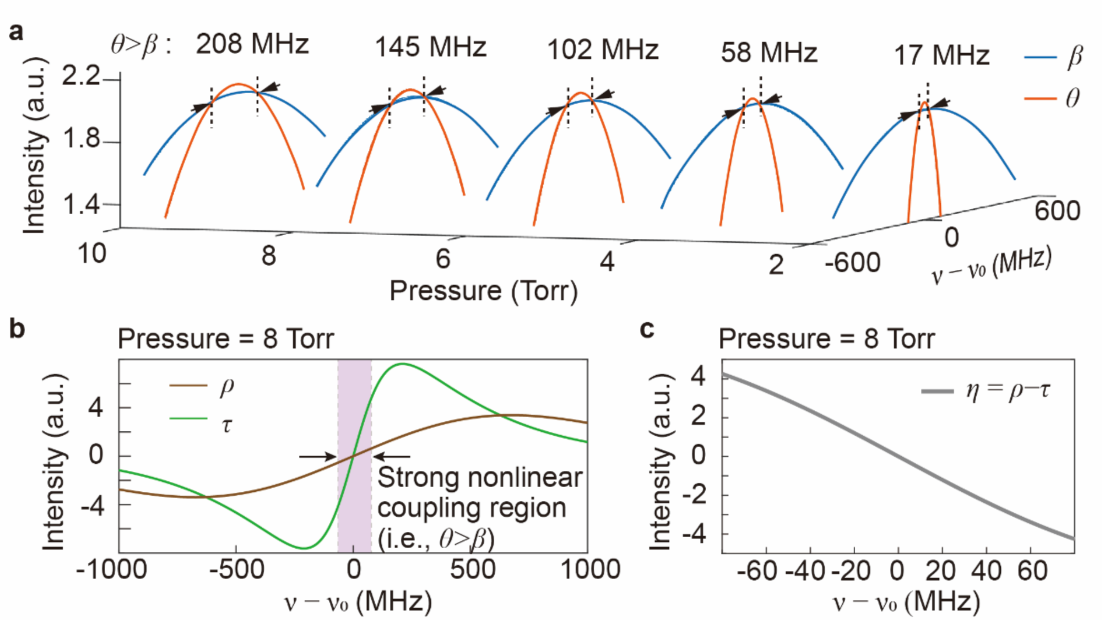

Fig. S1| Calculation of the nonlinear coefficients. **a**, Relative relationship between self- and cross-saturation coefficients (i.e., β and θ) versus laser frequency ν, for different gas pressure conditions. **b**, Self- and cross- pushing coefficients (i.e., ρ and τ) versus laser frequency ν at a pressure of 8 Torr. The purple-shaded region denotes the strong nonlinear coupling region. **c**, Differential value of self- and cross-pushing coefficients (i.e., nonlinear frequency pulling coefficient η) corresponding to the purple-shaded region in **b**.

As illustrated in Fig. S1**a**, the cross-saturation coefficients only exceed the self-saturation coefficients exclusively around the Ne^{20} gain center ν_0, defining the strong nonlinear coupling region ($\xi = \theta/\beta > 1$). Enhanced homogeneous broadening at elevated pressures substantially expands this region, resulting in a broader chiral tunability in He-Ne ring lasers. Notably, conventional He-Ne lasers operate at 1~3 Torr to maximize output power[4,5], where Doppler broadening dominates homogeneous broadening (i.e., Doppler-limited conditions), constraining $\xi \leq 1$. Thus, higher pressures (8~10 Torr) prove essential for realizing controllable chirality in this work.

According to equations (S4) and (S5), the nonlinear frequency pulling coefficient η can be written as:

$$\eta = \rho - \tau = -g\frac{c\kappa}{2L}\left[\frac{dZ_{\mathrm{i}}(\varepsilon)}{d\varepsilon} + \frac{\varepsilon}{\kappa^2 + \varepsilon^2}Z_{\mathrm{i}}(\varepsilon)\right] \tag{S6}$$

where g is the gain factor, c is the speed of light, L is the length of the laser cavity, κ is the ratio of the homogeneous broadening to Doppler broadening, $Z_{\mathrm{i}}(\varepsilon)$ is defined as the imaginary part of the plasma dispersion function $Z(\varepsilon)$, and ε is the frequency parameter. Figure S1**b** reveals S-shaped profiles of self- and cross- pushing coefficients ρ and τ, exhibiting odd-function symmetry with respect to ν_0. Within the strong nonlinear coupling region (i.e., $\xi > 1$ indicated by the purple shading), their quasi-linear variation versus $(\nu - \nu_0)$ as well as $|\rho| < |\tau|$ leads to a monotonically decreasing odd-function (i.e., nonlinear frequency pulling coefficient η) as shown in Fig. S1c.

S2: Analysis of the critical condition of chiral spontaneous symmetry breaking in a ring laser

In the main text, the calculation of the critical condition for chiral SSB neglects the effect of the rotation of the ring laser gyroscope, approximating the phase difference Δu in Equation (4) as zero. To validate this assumption, we tested the chiral SSB phase transition process under different rotation speeds and directions at a fixed operating frequency (i.e., $\nu = \nu_0$).

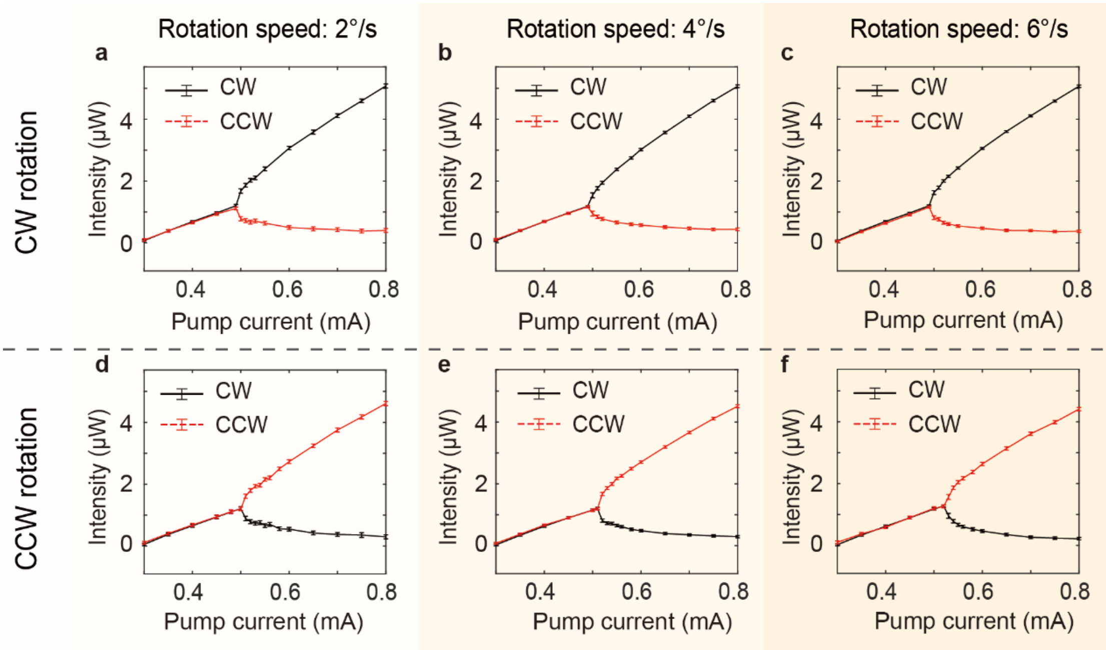

Fig. S2| Chiral SSB process of the ring laser gyroscope with various rotation speeds and directions at a fixed operating frequency. a~d, The output light intensities in the CW and CCW directions are shown as a function of increasing pump current. Panels **(a~c)** correspond to clockwise rotation of the gyroscope, where the CW intensity dominates after the phase transition; Panels **(d~f)** correspond to counter-clockwise rotation, where the CCW intensity dominates after the phase transition. Each column represents experimental results measured under different rotation rates.

As shown in Fig. S2, with increasing gain, the ring laser gyroscope undergoes a phase transition near a pump current of 0.5 mA under all rotation speeds tested. The change in rotation direction only leads to a flip in the chiral signature, which is consistent with the conclusions presented in the main text. The slight variations in the phase transition points across experiments are attributed to drifts in the operating frequency. This demonstrates that the rotation of the gyroscope does not affect the critical condition for chiral SSB.

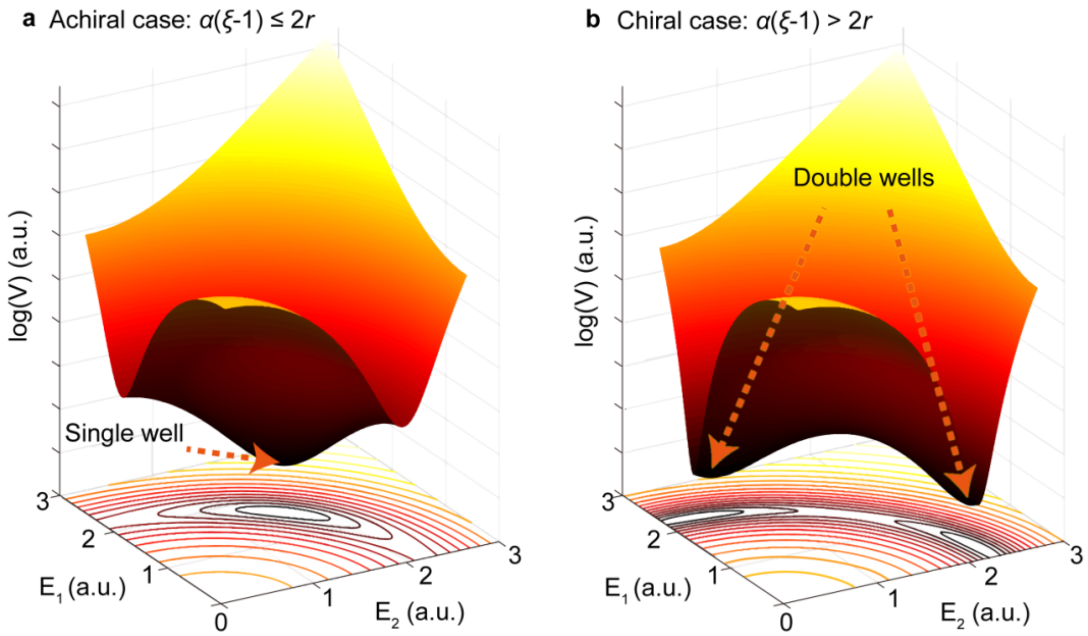

Fig. S3| Logarithmic plots of the two-dimensional potential function. **a**, Chiral case exhibits a single potential well. **b**, Achiral case exhibits double potential wells. α, ξ and r denote the net gain coefficient, the nonlinear coupling coefficient, and the backscattering coefficient, respectively.

Next, we will conduct a more in-depth analysis of the critical conditions for the phase transition. Equation (7) in the main text provides the critical condition of chiral spontaneous symmetry breaking: $\alpha(\xi-1) > 2r$, revealing the phase transition from a monostable state to a bistable state. This critical condition can be analyzed through the potential function[6,7] of E_1 and E_2:

$$\begin{aligned} \mathrm{V}(E_1, E_2) &= \int \dot{E}_1 dE_1 + \int \left[\dot{E}_2 - \left(\frac{\partial}{\partial E_2}\int \dot{E}_1 dE_1\right)\right] dE_2 \\ &= \frac{1}{4}\beta(E_1^4 + E_2^4) + \frac{1}{2}\xi\beta E_1^2 E_2^2 - \frac{1}{2}\alpha(E_1^2 + E_2^2) - rE_1E_2 \end{aligned} \quad \text{(S8)}$$

where E_1 and E_2 are field amplitudes of the CW and CCW modes; $\dot{E}_1 = E_1\big(\alpha - \beta(E_1^2 + \xi E_2^2)\big) + rE_2$ and $\dot{E}_2 = E_2\big(\alpha - \beta(E_2^2 + \xi E_1^2)\big) + rE_1$ are defined according to equation (3) from the main text; α, β, ξ, and r denote the net gain coefficient, the self-saturation coefficient, the nonlinear coupling coefficient, and the backscattering coefficient, respectively.

It can be readily verified that when the critical condition of chiral spontaneous symmetry breaking is satisfied, the extrema of the potential function $V(E_1, E_2)$ bifurcate from a single point into three distinct critical points, manifesting as a potential barrier flanked by two potential wells, as illustrated in Fig. S3. This geometric transition of the potential function vividly captures the evolution before and after the emergence of chirality. Within the spontaneous symmetry breaking phase, the depth of the double-well potential increases with both the net gain coefficient α and the nonlinear coupling coefficient ξ. Consequently, under low net gain or weak coupling conditions, minimal perturbations[8,9] (e.g., laser spontaneous emission noise) may trigger chirality switching.

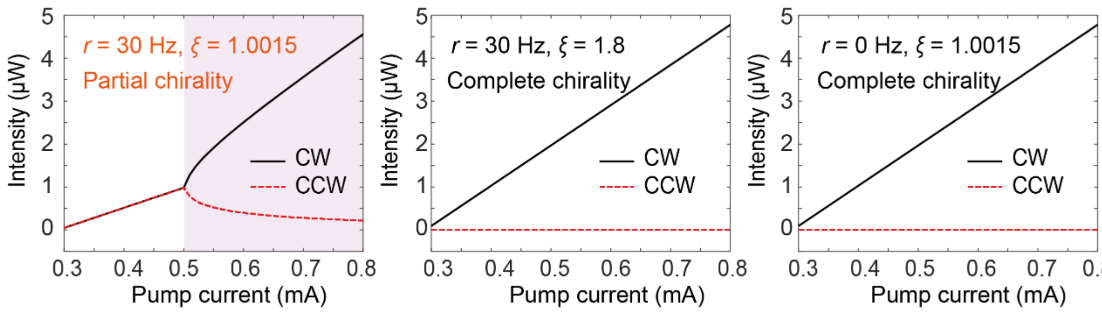

Fig. S4| Simulations of chirality features under different parametric configurations. α, ξ, and r denote the net gain coefficient, the nonlinear coupling coefficient, and the backscattering coefficient, respectively. The black solid lines / red dashed lines represent the intensity of the CW/CCW laser modes.

The net gain coefficient α represents the difference between gain and loss. Since an excessive pump current may induce the breakdown of the He-Ne gas, *minimizing cavity loss becomes critical for achieving stable chirality*. On the other hand, as depicted in Fig. S4**b**, excessively strong nonlinear coupling induces unidirectional lasing (i.e., complete chirality), wherein the laser mode in one direction extinguishes completely, thus losing the beat signal. Furthermore, a finite backscattering coefficient r proves necessary for the realization of partial chirality[10,11]. As shown in

Fig. S4**c**, vanishing backscattering also drives the ring laser into complete chirality. Thus, the *chiral-biased ring laser gyroscope* demonstrated in our work essentially arises from *a delicate balance between nonlinear coupling* (governed by ξ) *and linear coupling* (governed by r) under an ultra-low-loss condition.

S3: Control strategies of the chiral RLG based on its output signal

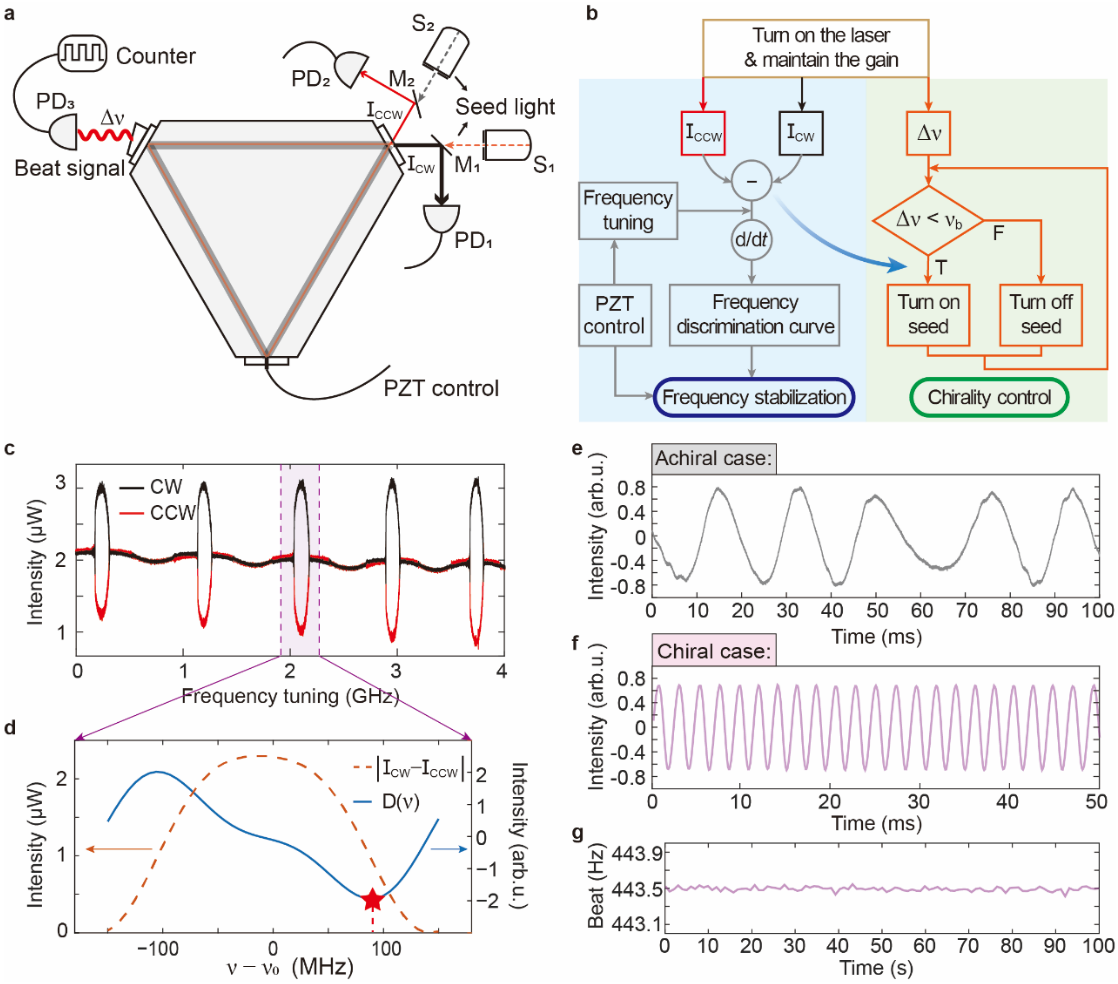

Fig. S5| Raw output signals and control strategies of the chiral RLG. **a**, Schematic of the signal readout and chirality control for the chiral RLG. PD1, PD2, and PD3 are photodetectors, measuring the CW laser intensity (I_{CW}), CCW laser intensity (I_{CCW}), and the beat signal $\Delta\nu$, respectively. The beat signal is then shaped and fed into a frequency counter. M_1 and M_2 are beam splitters. S_1 and S_2 are the seed sources. PZT: piezoelectric transducer. **b**, Flowchart of the frequency stabilization and chiral control protocol. **c**, Full-range frequency tuning curves of laser intensity under clockwise rotation at 0.04 °/s. Black and red curves represent the output power in the CW and CCW directions, respectively. The periodic pattern of chiral SSB indicates traversal of multiple longitudinal mode spacings during the unidirectional sweep of the PZT. Attributed to the clockwise rotation direction, the RLG consistently favors the chiral state with stronger CW mode intensity during cavity length tuning. **d**, Evolution of the intensity difference (orange curve) and the corresponding discrimination signal $D(\nu)$ (blue curve) as a function of laser frequency. The red star denotes the minimum of $D(\nu)$. **e**, Beat signal at a rotation rate of 0.04 °/s when the RLG is in the achiral state. **f**, Beat signal at the same rotation rate (0.04 °/s) when the RLG is in the chiral state. **g**, Continuous beat frequency over 100 seconds when the RLG is operated at the chiral state and stabilized at the point marked by the red star in panel **d**.

Maintaining the stability of the operating point and the chiral state is crucial for acquiring high-quality experimental data from the laser gyroscope. Figures S5**a** and S5**b** illustrate the experimental setup and the control methodology, respectively. The frequency stabilization scheme and the chiral control protocol are detailed below:

Frequency Stabilization Method: When the laser is turned on, the PZT is first swept unidirectionally. The DC photodetectors PD1 and PD2 simultaneously record the intensities of the CW and CCW laser modes, yielding the full-range mode sweeping curves (Fig. S5**c**). Concurrently, the absolute value of the intensity difference, $\Delta I = |I_{\mathrm{CW}} - I_{\mathrm{CCW}}|$, is computed in real-time via logic circuits. After noise reduction of the raw data, the corresponding PZT control voltages (V_i) at the extremum points of ΔI are recorded. The median, V_0, of these voltages is identified.

Subsequent fine frequency stabilization is performed around V_0. The orange curve in Fig. S5**d** shows the intensity difference ΔI around V_0; and the blue curve, the discrimination signal $D(v)$, is its derivative with respect to time, and is used for frequency stabilization. The discrimination signal $D(v)$ is processed (smoothed and amplified) to precisely locate its minimum (red star, Fig. S5**d**). During operation, the frequency of the RLG (i.e., the operating point) is locked to this minimum by finely adjusting the PZT (displacement ~1 nm).

The sum of I_{CW} and I_{CCW} is also monitored in real-time to maintain gain stability by keeping the total intensity constant.

Chiral Control Method: Chiral state switching is induced via seed light injection. As shown in Fig. S5**a**, weak seed lights from S_1 and S_2 are injected into the CCW and CW directions via beam splitters M_1 and M_2, respectively. When the gyro is under frequency stabilization, the beat frequency and CW/CCW laser intensities are monitored in real-time. If the beat falls below a predefined bias frequency ν_b (determined by prior calibration), a chiral switch is then triggered. Based on the real-time intensity information, a seed light is injected into the direction with weaker intensity to promote a transition back to the desired chiral state.

Signal Output Analysis: Figures S5**e** and S5**f** display the raw beat note signals detected by an AC-coupled photodetector (PD3) when the RLG is operating at the achiral point and the chiral stabilization point (i.e., red star in Fig. S5**d**), respectively. The rotation speed of the RLG is 0.04 °/s , which is close to the lock-in threshold of the achiral state. The raw beat signal under chiral conditions (Fig. S5**e**) exhibits a standard sinusoidal waveform with a significantly high signal-to-noise ratio. In contrast, under the achiral state, because the rotation speed of the gyroscope is very close to its lock-in threshold, the raw beat signal (Fig. S5**f**) suffers from pronounced distortion, which substantially compromises the frequency stability of the gyroscope.

Commercial laser gyroscopes employ a mature frequency counting method (Fig. S5**a**, top left): the sinusoidal beat note is converted into a square wave and counted digitally. Therefore, variations in the AC signal amplitude due to asymmetric intensities in the chiral state do not affect the frequency measurement accuracy. Figure S5**g** shows a 100-second frequency recording at the stabilization point under a 0.04 °/s rotation. The standard deviation over 100 seconds is merely 0.1 Hz (approximately 0.1% of the beat signal), demonstrating high stability and minimal error.

S4: Analysis of bias stability in the chiral ring laser gyroscope

The stability of this bias directly determines the gyroscope's bias instability. As calculated by the Allan deviation in Fig. 4**d** of the main text, the gyroscope's bias instability at 10 seconds under stationary conditions is 2.2×10^{-2} °/h, satisfying typical industrial application requirements.

Differing from the traditional achiral RLG, the frequency bias in the chiral RLG arises from spontaneous symmetry breaking. Given the unique nature of this biasing mechanism, we analyze the stability of the chiral RLG's frequency bias concerning two key factors influencing chiral SSB: laser frequency and gain.

Figure 4**a** in the main text shows the relationship between the frequency bias and laser frequency. Near the point of maximum bias, the change in bias induced by a shift in the operating point is relatively small: a frequency drift of 1 MHz corresponds to a bias change of approximately 2.8 Hz, which is less than 1% of the total bias. For the resonator with a perimeter of 375 mm in our work, a cavity length change of 1 nm corresponds to a bias shift of about 3 Hz. This level of control is readily achievable with PZTs offering nanometer-scale precision.

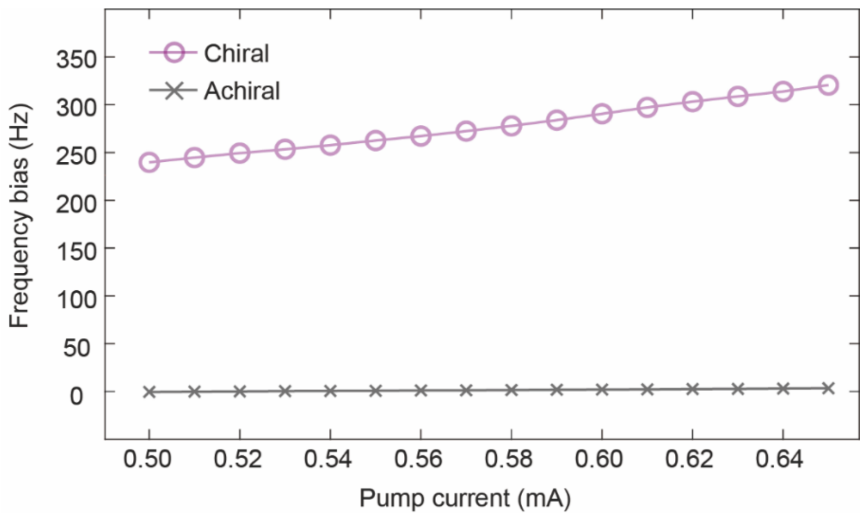

Fig. S6| Frequency drift of chiral and achiral RLGs under different pump currents

Figure S6 illustrates the impact of gain variation on the frequency bias. With the gyroscope stabilized at a certain operating point (i.e., the red star shown in Fig. S5**d**), the purple curve in Fig. S6 shows that increasing the current from 0.5 mA to 0.6 mA raises the frequency bias by about 50 Hz, correlating with an increased intensity asymmetry. Considering that current fluctuations from a stabilized power supply can be smaller than 1%, the corresponding fluctuation in the frequency bias is estimated to be around 2.5 Hz. In contrast, the beat frequency of the RLG in the achiral state is not affected by gain fluctuations.

In summary, for the chiral RLG presented in our work, typical frequency and gain drifts result in a variation of less than 1% in the frequency bias. Consequently, the chiral laser gyroscope imposes more stringent engineering requirements on gain stability and frequency stabilization methods compared to traditional laser gyroscopes.

S5: Operating characteristics of the He-Ne ring laser

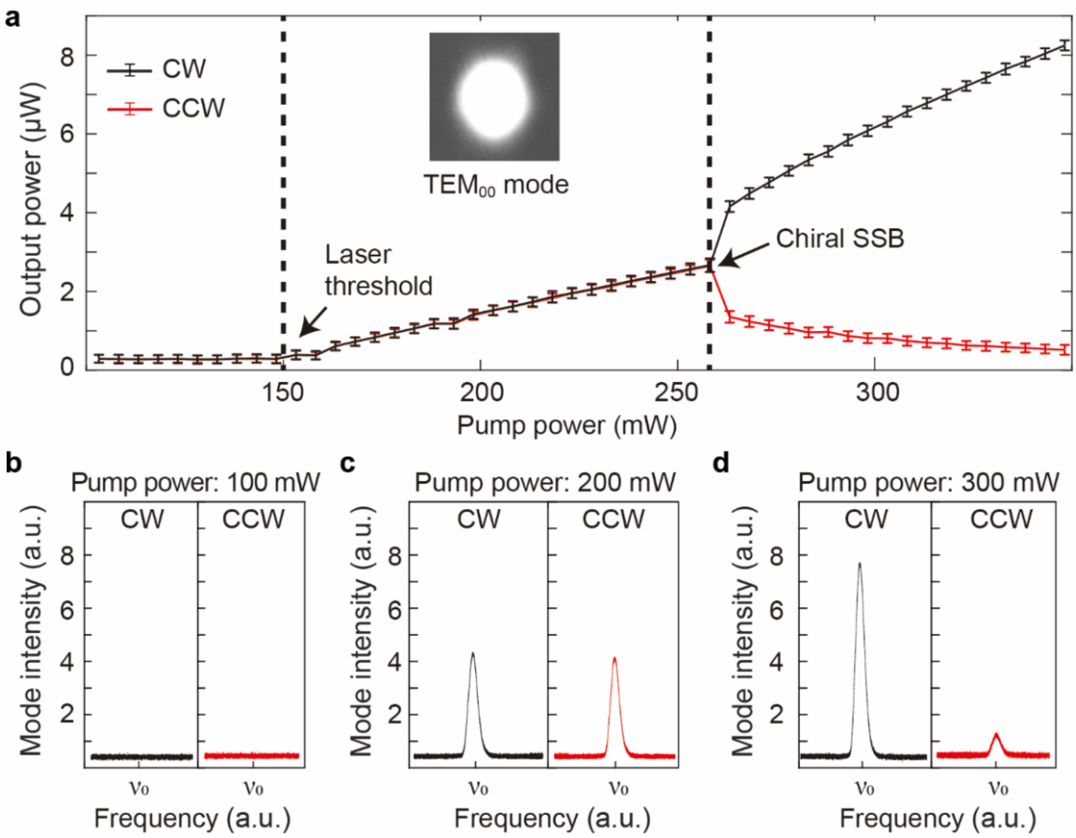

Fig. S7| Operating characteristics of the He-Ne ring laser under the strong-coupling condition. a, Evolution of the CW/CCW laser mode power versus pump power. Lasing initiates at the pump power of 150 mW, with output power scaling linearly until chiral SSB emerges at the pump power of 260 mW. Inset: Beam profile confirming the fundamental TEM_{00} mode. **b,** No lasing at the pump power of 100 mW. **c,** Symmetric single-longitudinal-mode operation in CW/CCW directions at the pump power of 200 mW. **d,** Asymmetric single-longitudinal-mode operation at the pump power of 300 mW. Here, ν_0 denotes the central resonance frequency of the laser.

As shown in Fig. S7**a**, the He-Ne ring laser exhibits a pump power threshold of 150 mW with a constant DC voltage of about 520 V, where the loss of the TEM_{00} mode is 68 ppm, measured via the cavity ring-down technique. Under the strong-coupling condition, chiral SSB emerges at pump powers exceeding 260 mW. Figures S7**b** and S7**c** present the mode characteristics measured by a Fabry-Pérot interferometer (FPI, SA30-57, Thorlabs) across three operational states: below threshold (100 mW pump power; no lasing output), above threshold (200 mW pump power; symmetric single-longitudinal-mode emission in counter-propagating directions), and within the chiral SSB state (300 mW pump power; the intensity of the CW mode is significantly stronger than that of CCW mode).

References:

1. Aronowitz, F. Effects of Radiation Trapping on Mode Competition and Dispersion in the Ring Laser. *Appl. Opt.* **11**, 2146 (1972).
2. Menegozzi, L. N. & Lamb, W. E. Theory of a Ring Laser. *Phys. Rev. A* **8**, 2103–2125 (1973).
3. Anh, T. D. & Dietel, W. Homogeneous broadening in a 0.63 μm single mode He-Ne laser. *Opto-electronics* **5**, 243–248 (1973).
4. Field, R. L. Operating Parameters of dc-Excited He-Ne Gas Lasers. *Rev. Sci. Instrum.* **38**, 1720–1722 (1967).
5. Petrů, F. & Veselá, Z. The output power of 633nm He-Ne lasers. *Opto-electronics* **4**, 1–20 (1972).
6. Iooss, G. & Joseph, D. D. *Elementary Stability and Bifurcation Theory*. (Springer New York, 1990). doi:10.1007/978-1-4612-0997-3.
7. Erneux, T. & Glorieux, P. *Laser Dynamics*. (Cambridge University Press, 2010). doi:10.1017/CBO9780511776908.
8. Tredicce, J. R., Arecchi, F. T., Lippi, G. L. & Puccioni, G. P. Instabilities in lasers with an injected signal. *J. Opt. Soc. Am. B* **2**, 173 (1985).
9. Sorel, M. *et al.* Alternate oscillations in semiconductor ring lasers. *Opt. Lett.* **27**, 1992 (2002).
10. Spreeuw, R. J. C., Neelen, R. C., van Druten, N. J., Eliel, E. R. & Woerdman, J. P. Mode coupling in a He-Ne ring laser with backscattering. *Phys. Rev. A* **42**, 4315–4324 (1990).
11. Cheng, F. C. Investigation of a dye ring laser with backscattering. *Phys. Rev. A* **45**, 5220–5227 (1992).